

3D Nanoscale Characterization of Thin-Film Organic Photovoltaic Device Structures via Spectroscopic Contrast in the TEM

Andrew A. Herzing,* Lee J. Richter,[†] and Ian M. Anderson[‡]

Surface and Microanalysis Science Division, National Institute of Standards and Technology, Gaithersburg, Maryland, United States

Received: June 25, 2010; Revised Manuscript Received: August 17, 2010

The three-dimensional characterization of third generation photovoltaic device structures at the nanometer scale is essential to the development of efficient, reliable, and inexpensive solar cell technologies. Electron tomography is a powerful method for three-dimensional characterization; however, the application of this method to the organic materials systems that comprise typical high-efficiency devices is complicated by the difficulty in generating contrast from the compositionally similar materials. Herein we report the application of low-loss energy-filtered transmission electron microscopy as a method of generating spectroscopic contrast from a common organic bulk-heterojunction thin film consisting of a polymer donor and a fullerene-derivative acceptor. Spectral imaging methods combined with principal component analysis are used to characterize the contrast generation mechanism and to determine the optimum data acquisition parameters for this particular combination of organic phases. A proof of method for using the low-loss spectral signal as a basis for electron tomography is presented, and the advantages and drawbacks of the technique as applied to multiphase organic systems relative to the more commonly employed bright-field imaging approach are outlined.

1. Introduction

A promising route to implementing a shift in the world's energy usage to renewable sources is the development of low-cost, mass-produced, third-generation photovoltaic (PV) devices.¹ Encouraging performance has been achieved by organic solar cells based on bulk-heterojunction (BHJ) thin film structures consisting of an interpenetrating network of two organic phases, acting respectively as electron donor and acceptor materials. Specifically, BHJ thin film devices based on a donor/acceptor combination of regioregular poly(3-hexylthiophene) (P3HT) and a [6,6]-phenyl C61 butyric acid methyl ester (PCBM) fullerene derivative have exhibited external quantum efficiencies as high as 75% and power-conversion efficiencies (PCE) of ~4%.² The development of alternate polymer acceptors has led to PCEs above 6%.³ The high performance of the BHJ architecture has been attributed to the nanometer-scale self-assembly of heterojunctions formed by spontaneous phase separation of the two constituents.⁴ Improving the efficiency of such multiphase devices depends upon understanding and exploiting their inherent structural, chemical, and electronic heterogeneities. Since these features are organized in a complex, highly interconnected three-dimensional (3D) network at length scales that are typically on the order of tens of nanometers, their proper characterization represents a difficult challenge from a measurement science perspective.

Electron tomography in the transmission electron microscope (TEM) is a proven method for characterizing the three-dimensional morphology of heterogeneous materials at nanometer length scales.⁵ Recent studies have applied electron tomography to the analysis of the 3D morphology of organic BHJ thin films using conventional bright-field (BF) TEM

imaging.^{6–8} However, the organic phases such as P3HT and PCBM that comprise BHJ systems typically exhibit low differential contrast due to their similarities in composition. In these studies, phase contrast has been enhanced by imaging with a defocused objective lens, thereby tuning the contrast transfer function to emphasize a narrow band of spatial frequencies that correspond to the predominant length scale (≥ 10 nm) of the phase separation. However, this contrast enhancement strategy presents significant drawbacks for the 3D analysis of the distributions of the donor and acceptor phases in these device structures. First, the large defocus degrades the intrinsically high spatial resolution of the TEM, necessarily blurring structural detail at length scales smaller than the selected bandpass; hence this approach may discard relevant information related to features at these length scales which may significantly affect device properties. More significantly, defocused BF images are dominated by phase contrast, which does not necessarily obey the fundamental assumption upon which tomographic reconstruction methods are based, namely that the acquired signal varies monotonically with the integrated mass thickness of the relevant phase.⁹ However, BF *amplitude* contrast, which is often enhanced in organic structures via the practice of selective “staining” of a phase or feature with a high atomic number atom, does obey the projection requirement with an intensity variation governed by Beer's Law.⁹ In this latter case, imaging is performed at Gaussian focus (i.e., with no defocusing of the objective lens), thus preserving the subnanometer spatial resolution of TEM and allowing the characterization of the complex 3D morphology at all relevant length scales. Clear evidence of the failure of TEM *phase* contrast imaging to meet this requirement is the well-known Fresnel fringe—bright or dark depending upon whether the objective lens is under- or overfocused—that appears at the edge of the specimen; for example, current generation tomographic reconstruction algorithms would interpret the bright fringe in a traditionally

* To whom correspondence should be addressed. E-mail: andrew.herzing@nist.gov.

[†] E-mail: lee.richter@nist.gov.

[‡] E-mail: ian.anderson@nist.gov.

underfocused image as a mass thickness *lower than that of the adjacent vacuum*, which is unmistakably an artifact.

Spectroscopic imaging via energy-filtered TEM (EFTEM) provides an alternative contrast generation mechanism for tomographic analysis that does not suffer from the drawbacks of BF phase contrast imaging. EFTEM imaging is performed at Gaussian focus, as the image contrast results from the intrinsic differences in chemistry or electronic structure between the phases.¹⁰ In recent years, chemical imaging of organic materials via EFTEM imaging has become increasingly popular. For example, the microstructure of multiphase systems has been probed via core-loss elemental mapping,^{11–15} and the spatial distribution of carbon bonding states in a triphase polymer composite has also been mapped.¹⁵ In addition, this spectroscopic signal obeys the projection requirement for specimens whose thickness is small in comparison with the inelastic mean free path (~ 100 nm) of the incident electrons,¹⁶ and the utility of EFTEM-based imaging for tomography of polymer/carbon nanotube composites¹⁷ and block copolymers¹⁸ has been demonstrated.

In this work, the applicability of EFTEM low-loss imaging to the structural and chemical characterization of organic PV device structures will be demonstrated on a widely studied BHJ thin film system consisting of P3HT and PCBM. The advantages and drawbacks of this approach relative to the more widely used techniques based on bright-field TEM imaging will be discussed, and its applicability to high spatial resolution 3D characterization of organic PV device structures will be demonstrated.

2. Experimental Section

2.1. Specimen Preparation. The protocol for synthesizing the BHJ device structures considered here has been described in detail elsewhere.¹⁹ Briefly, a thin film BHJ sample comprised of P3HT and PCBM (Plexcore 2100, Plextronics Inc. and Nano-C Inc., respectively) was prepared from a solution of the two phases dissolved, in equal proportions by mass, in 1,2-dichlorobenzene.²⁰ The solution was spin-coated onto a glass substrate supporting a film of indium tin oxide (ITO) and a 40-nm-thick sacrificial layer of poly(3,4-ethylenedioxythiophene) poly(styrenesulfonate) (PEDOT:PSS). A slow drying procedure¹⁸ was used to produce a BHJ that had previously been found to exhibit power conversion efficiencies of greater than 2%.²¹ For analysis of the films by TEM, the specimens were scored and immersed in water to promote dissolution of the PEDOT:PSS layer. The delaminated film was then floated onto a copper TEM grid. In addition, films of the individual constituent phases (i.e., PCBM and P3HT) were similarly prepared.

2.2. Electron Microscopy and Tomography. The three thin-film samples (hereafter denoted P3HT, PCBM, and BHJ) were analyzed via electron-energy loss spectroscopy (EELS) in an FEI Titan 80–300 TEM/STEM operating at 80 kV and equipped with a Gatan Model 865 Tridiem imaging energy filter. To prevent potential degradation of the EELS spectral features, the preliminary EELS analysis was carried out using a Gatan Model 626 cryo-transfer TEM holder. The sample was cooled to -130 °C and allowed to stabilize at this temperature for several minutes prior to exposure to the electron beam.

EFTEM spectral imaging (SI) was performed using an energy selecting slit of width $\Delta E = 2$ eV and an energy increment (step size) of $\delta E = 0.2$ eV, thereby providing an oversampling $\Delta E/\delta E = 10$. An EFTEM-SI image series was acquired across the low-loss (LL) region of the spectrum, comprising the zero-loss (ZL) peak and the plasmon-loss resonance, in the energy

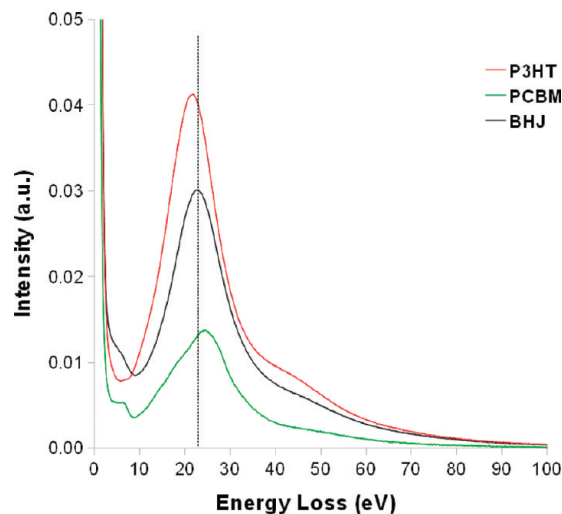


Figure 1. EELS spectra acquired from the P3HT, PCBM, and BHJ films. The dashed line overlays the maximum of the plasmon peak for the BHJ film, showing that it is present at an energy loss between the plasmon peaks of the two pure materials. A weak spectral feature at an energy loss near $E = 6$ eV is present in the spectra acquired from both the PCBM standard and the BHJ film.

loss range -5 eV $\leq E \leq 40$ eV, thereby producing a data cube of 225 images. The data were acquired with 0.5 s exposures with the (2048 \times 2048) pixel camera configured for a 4 \times on-chip binning to produce (512 \times 512) pixel images with a sampling of ~ 2 nm/pixel and a field of view of ~ 1 μ m as measured in the plane of the sample. The data cube was filtered in order to remove point blemish artifacts such as X-rays and, if necessary, registered to correct for spatial drift using the FELMI plug-in for Digital Micrograph.²² Finally, the data cube was analyzed by principle component analysis (PCA) using the AXSIA²³ SI analysis program operating on a desktop PC.

EFTEM tomography analysis of the thin-film BHJ was performed at room temperature using a Fischione Instruments model 2020 high-tilt tomography holder. A series of 141 EFTEM images were acquired using a Saxton scheme (tilt increment = 1.5° at 0° tilt) over a specimen tilt range of $-70^\circ \leq \theta \leq +70^\circ$ using the FEI Xplore3D tomography acquisition software. All images were acquired using an energy-selecting slit $\Delta E = 5$ eV centered at $E = 19$ eV on the low-energy shoulder of the bulk plasmon peak for the BHJ, which had been identified during EFTEM-SI analysis as providing optimal contrast between the constituent phases. Images were acquired using a 2 s integration time and a 2 \times on-chip binning to produce (1024 \times 1024) pixel images with a sampling of approximately 1 nm. A second EFTEM tilt series was acquired from a different portion of the film under identical conditions, except in this case the energy-selecting slit was centered at $E = 0$ eV on the zero-loss peak, with an objective lens defocus of -25 μ m, in order to enhance the inherently low contrast in this imaging mode. The raw image stacks were then registered to the common tilt axis by multiple iterations of cross-correlation analysis and subsequently reconstructed using the weighted-back-projection algorithm in the IMOD tomography reconstruction software.²⁴

3. Results and Discussion

EELS spectra acquired from the single component films of P3HT and PCBM, as well as the BHJ device structure are shown in Figure 1. The spectra of all three films exhibit broad plasmon-loss resonances with peak intensities near 25 eV; however, the three samples exhibited subtle variations in peak energy and

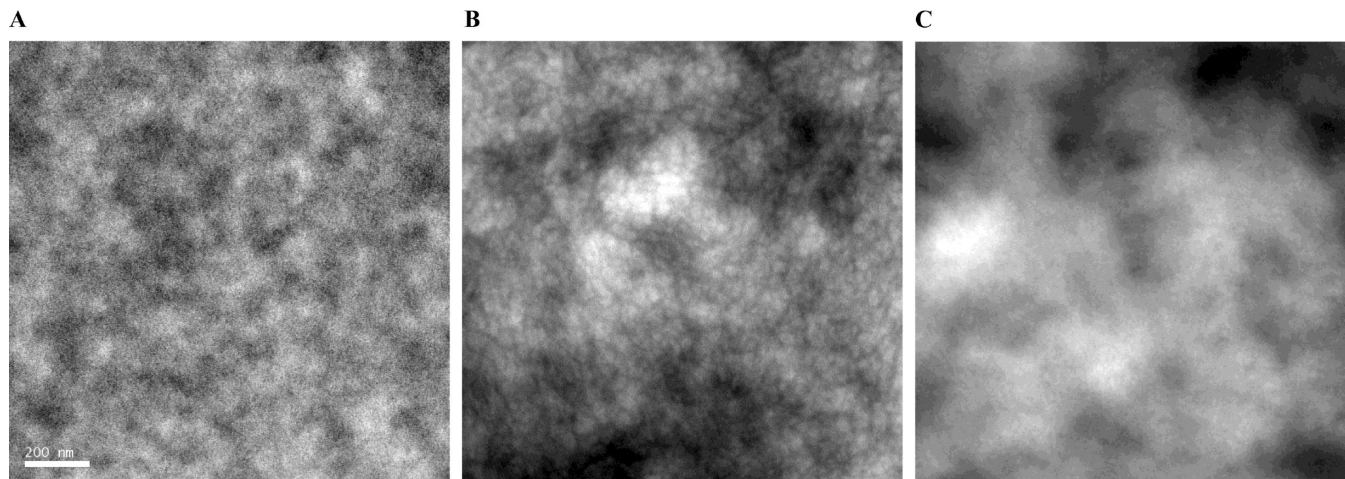


Figure 2. Typical zero-loss BF images ($E = 0$ eV, $f = 0$ μm) of the (a) PCBM, (b) P3HT, and (c) BHJ films. Note the large domains present in the P3HT and the difficulty in discerning contrast between the two constituents in the BHJ film. The scale bar is 200 nm.

shape. For the P3HT film, the plasmon peak energy is found to be 22.2 eV, while that of the PCBM film is at 25.5 eV. The relative values are consistent with the decreased electron density of the polymer compared with the fullerene derivative.²⁵ The plasmon peak energy of the BHJ device structure lies between the two values exhibited by the individual components, at 23.3 eV.

Two other features of note are evident in the EELS spectrum of the PCBM phase. First, a minor but distinct peak is found at ~ 6.6 eV. This feature has been attributed to the π -plasmon excitation of the C_{60} molecule.^{26,27} Second, the low-energy shoulder of the PCBM plasmon peak deviates noticeably from the quasi-Gaussian shape exhibited by the P3HT and the bulk plasmon peaks of most materials. This distinctive shape is due to additional interband transitions of valence electrons to the σ^* band,^{26,27} which within the limited spectral resolution of this analysis (~ 0.7 eV) appears as an approximately linear increase in the spectral intensity over a 15 eV energy range between the local minimum at around 9 eV and the plasmon intensity maximum. The first of these two spectral features, which is also apparent in the BHJ device structure, provides a useful indicator of the spectral signature of the fullerene derivative.

Representative EFTEM zero-loss bright-field images of the three films, each acquired at Gaussian focus, are shown in Figure 2. The zero-loss image of the PCBM film is largely featureless at this magnification. Conversely, the P3HT exhibits equiaxed domains which are several tens of nanometers in diameter; a morphology that is consistent with previous AFM studies of P3HT.²⁸ Also evident are macroscopic thickness variations, evident as low-frequency variations in intensity across the image, that are largely absent in the image of the PCBM film. Most significantly, the image of the BHJ device structure demonstrates the difficulty in generating contrast that distinguishes between the polymer and fullerene phases using bright-field zero-loss imaging at Gaussian focus due to the intrinsically low amplitude contrast differentiating between these compositionally similar phases. Instead, the image contrast is dominated by low-frequency intensity variations due to film thickness, similar to that seen in the P3HT film.

Given the low intrinsic amplitude contrast between the P3HT and PCBM phases in the TEM BF images, the difference in the spectral signatures of the two phases was explored as an alternative source of contrast generation. To correlate the spectral features of the two constituent phases with their spatial distribution in the BHJ devices, an EFTEM spectral image,

comprised of a full spectrum such as those shown in Figure 1 for each imaging point (pixel), was acquired from the BHJ specimen. To a first approximation, the spectral response from any individual imaging point might be expected to be a linear combination of the spectral responses of the individual phases shown in Figure 1. However, deviations from this linear behavior may arise for a variety of reasons. For instance, charge transfer between the donor and acceptor phases in the BHJ may result in a qualitative change in the dielectric response relative to the single-phase standards, producing either a change in sensitivity factor or a modification in spectral shape. Alternatively, the segregation of charge to the interface may give rise to a distinct interfacial component to the dielectric response. Since our goal is to use the low-loss EFTEM signal as the basis for quantifying the relative proportions of the constituent phases in projection, a prerequisite for tomographic analysis, it is essential that the spectroscopic signal and its relationship to the constituent phases be well understood.

Multivariate statistical methods, such as principal component analysis (PCA), can be used as a means to understand the origin of the features in a spectral image. The details of PCA and its application to microanalysis in general and EFTEM specifically have been described in detail elsewhere.^{23,29,30} Briefly, PCA identifies a minimal basis set of spectral components, a linear combination of which accurately reconstructs the spectral response at each pixel of the SI, apart from the contribution of statistical noise. The analysis reveals the number of linearly independent components distinct from the noise, so that spectral variations arising from unexpected sources in the specimen (e.g., a distinct interfacial component, as hypothesized above) or in the instrumental response (e.g., a detector nonlinearity) are reliably identified. Each component consists of a component spectrum, showing the nature of the distinct spectral variation, and a component image, which provides a real space map of the regions of the specimen where this spectral variation occurs. The combination of the component spectrum and image typically allows the origin of the extracted spectral variations to be identified. Moreover, because PCA identifies the intrinsic spectral variations within the SI itself, any alteration of the spectral response in the real structure relative to single phase standards (e.g., due to charge transfer) is automatically accounted for.

The application of PCA to the EFTEM SI acquired from the BHJ thin films revealed six components distinct from the contributions of Poisson noise. Component 1 describes the average

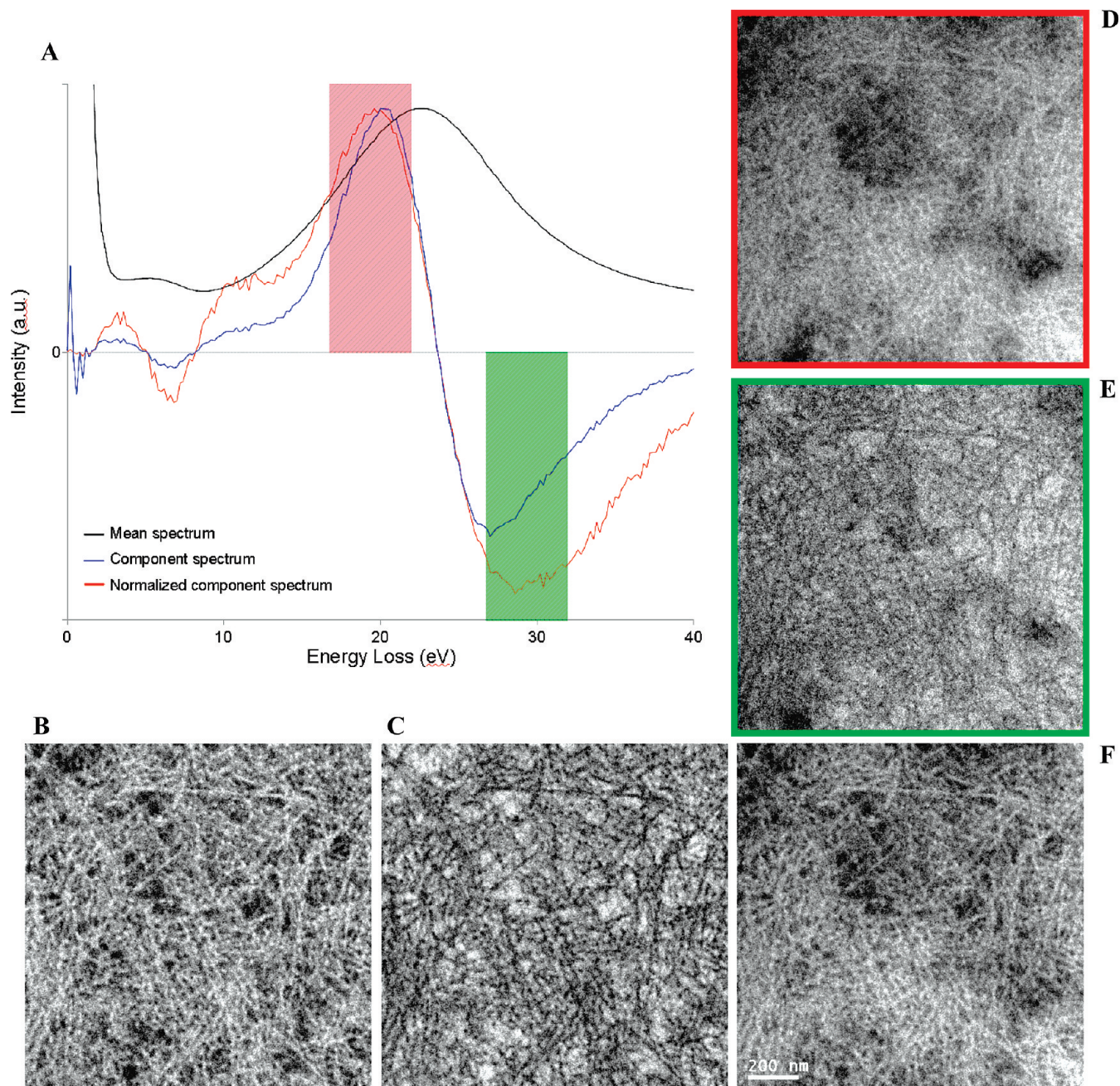


Figure 3. Results of the PCA analysis of the BHJ EFTEM-SI data cube: (a) spectral component that describes chemical contrast between the P3HT and PCBM phases; (b) component image corresponding to (a), highlighting P3HT; and (c) component image with inverted contrast, highlighting PCBM. Also shown are the raw images extracted from the data cube centered at (d, red border) $E = 19$ eV and (e, green border) $E = 29$ eV, the energies corresponding to the extrema in (a), as well as (f) the difference of images (d) and (e), depicting the maximum contrast difference of any pair of images in the EFTEM-SI. Image (f) provides a good approximation to image (b), but with lower absolute contrast given that the SI component image integrates contrast throughout the entire spectral range. The scale bar is 200 nm.

spectral response, with a spectral intensity distribution similar to that shown for the BHJ in Figure 1. Components 2, 3, and 5 correspond to the detector response, arising because of spectral shifts or broadening at the periphery relative to that in the center of the detector. Component 4 corresponds to variations in specimen thickness, with an image component exhibiting an intensity distribution similar to that in Figure 2c. Component 6 describes the difference in spectral response between the P3HT and PCBM phases in the BHJ thin film. Significantly, no additional spectral components (arising from, for example, an interfacial response distinct from that of the constituent phases) were identified.

Selected results of the PCA analysis of the EFTEM SI are shown in Figure 3. Spectral components 6 and 1, as well as

their ratio, are plotted in Figure 3A. Spectral component 6 exhibits the positive and negative intensities characteristic of PCA spectral components with index (n) greater than 1. This arises because the intensity distribution in these spectral components is relative to the mean spectrum, which is represented by component $n = 1$. In the present case, the positive portion of spectral component 6 consists of a single extrema near 19 eV loss, while the negative portion exhibits an extrema near 27 eV as well as a minor component at ~ 6.6 eV loss. This intensity distribution can be understood by comparison with the spectra acquired from the single phase P3HT and the PCBM films shown in Figure 1. The minor component at 6.6 eV combined with the higher energy-loss value of the extrema indicates that, to a good approximation, the negative portion

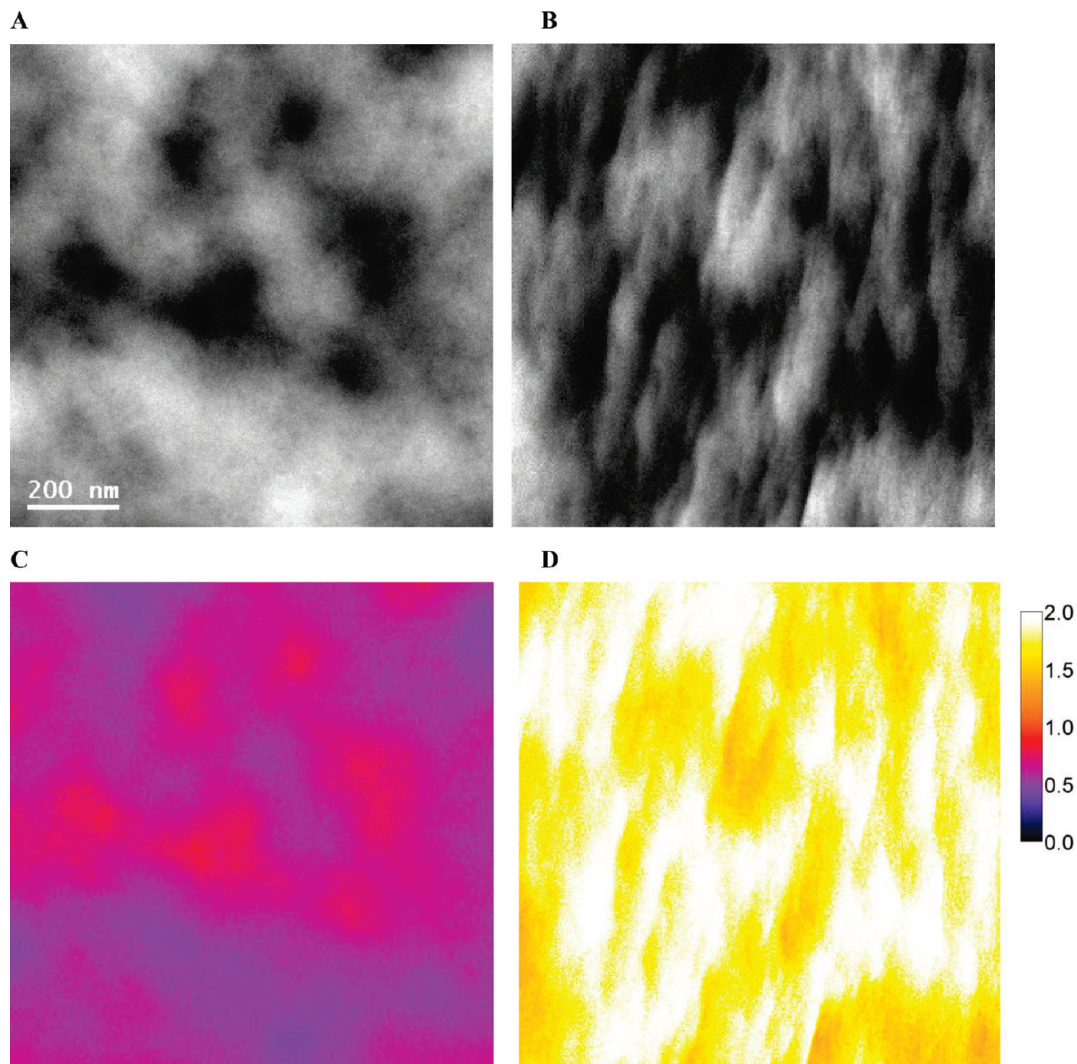


Figure 4. Zero-loss BF images (top, $E = 0$ eV, $f = 0$ μm) and thickness maps (bottom) obtained from an BHJ film at specimen tilts of (a,c) $\theta = 0^\circ$ and (b,d) $\theta = 70^\circ$. The thickness maps are shown on a false color scale with black corresponding to zero thickness and white corresponding to a thickness of two inelastic mean free paths.

corresponds to the PCBM, while the positive portion, with the lower energy loss extrema, corresponds to the P3HT. Thus component 6 represents the *signal* that distinguishes the two phases.

For the purposes of identifying optimal imaging characteristics for subsequent analysis, the more salient spectral distribution is the ratio of spectral components 6 and 1, since this provides a measure of *contrast*. Relative to the “signal,” the “contrast” spectral component exhibits intensity extrema of greater energy-loss separation, an enhancement of the spectral feature characteristic of the fullerene derivative at ~ 6.6 eV, and a suppression of the noisy intensity fluctuation below the zero loss peak. The 5-eV-wide intervals, which represent the spectral signals that would produce the greatest contrast in the P3HT and PCBM phases, are found to be centered at 19 and 29 eV, respectively, and these regions are highlighted by the overlain red and green windows.

The image component that corresponds to spectral component 6, and its complement, are shown in Figure 3, parts B and C, respectively. In the former image, regions of high intensity represent pixels which correspond to the positive (i.e., P3HT) portion of spectral component 6, while in the latter the high intensity pixels correspond to the negative (PCBM) portion. The image component associated with enhanced P3HT exhibits a

filament-like structure, while that associated with enhanced PCBM highlights an equiaxed morphology that occupies the channels bounded by the filaments. These structural characteristics of the two BHJ constituents are consistent with previous cryogenic BF-TEM imaging studies that reported a microstructure consisting of elongated, filament-like crystals of P3HT in a matrix of PCBM.⁶

For comparison, the two image slices corresponding to the red and green windowed energy regions in the “contrast” spectral component were extracted from the unprocessed 225-image EFTEM SI data set, and these are presented in Figure 3, parts D and E. The intensity difference between these two ‘raw’ images is also shown in Figure 3F. The intensity difference is similar to the component image in Figure 3B, but with a lower signal-to-noise ratio. Similarly, the individual image slices of Figure 3, parts D and E exhibit intensity variations similar to the component images of Figure 3, parts B and C, respectively, but with lower overall signal and contrast. The difference in these component images and the extracted raw images arises because PCA of spectral images effectively provides noise filtering by integrating the spectral difference throughout the image stack. Nevertheless, Figure 3, parts D and E, provide sufficient discrimination between the P3HT and PCBM phases to merit further imaging of the nanoscale microstructure of the

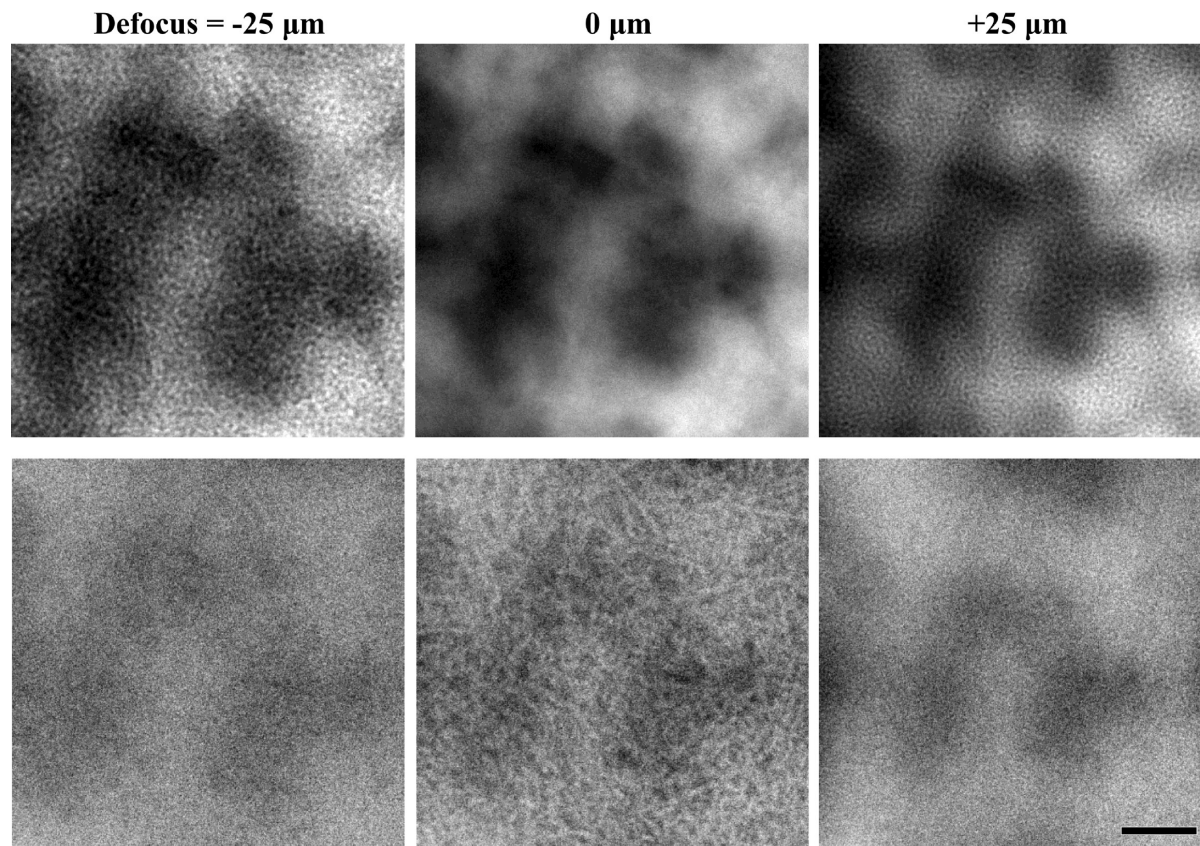


Figure 5. EFTEM image series array acquired at varying energy losses (E) and defocus (f): the rows (top to bottom) show images acquired with energy selecting slit centered on $E = (0 \text{ and } 19) \text{ eV}$; the columns (left to right) show images acquired with an objective lens focus of $f = (-25, 0, \text{ and } +25) \mu\text{m}$. The scale bar is 200 nm. Low-frequency thickness-related variations in intensity are present in all of the images; however, intensity variations arising from compositional inhomogeneity is clearly revealed only in the low-loss EFTEM images acquired at Gaussian focus. Note that there are high-frequency modulations in image intensity in the defocused zero-loss bright field images but that the apparent structure is distinctly different from that apparent in the lowloss images. A movie showing the entire data set for all three imaging conditions is included in the Supporting Information.

BHJs with these individual energy-filtered images, since their acquisition is simpler and more dose efficient than a full SI series. More importantly, for 3D characterization by tomography, this imaging paradigm provides the critical advantages of speed and a total signal that is proportional to a linear combination of the mass thickness of the individual phases.

Once the optimal EFTEM imaging conditions had been identified, it was necessary to evaluate the suitability of the plasmon-loss signal for acquisition of images at the specimen tilts, θ , required for electron tomography. The linearity of the EFTEM signal can be degraded by nonlinear plural plasmon scattering events at projected thicknesses greater than the electron inelastic mean-free path, λ . Since all TEM images are necessarily projections through the thickness of the specimen, this effect could be particularly limiting at high specimen tilts, where the projected thickness of a parallel-sided thin film increases inversely proportional to $\cos(\theta)$. It is well established that a map of the ratio of the specimen thickness to the inelastic mean-free path (t/λ), can be formed from the ratio of bright-field images acquired with and without an energy-selecting slit that excludes electrons that have undergone inelastic scattering.³¹ Bright-field images and t/λ maps of BHJ thin films at tilt angles of $\theta = 0^\circ$ and $\theta = 70^\circ$ are shown in Figure 4. At $\theta = 0^\circ$, the BHJ film is well suited to EFTEM analysis, with mean and maximum t/λ values smaller than 0.4 and 0.8, respectively. These values necessarily increase at $\theta = 70^\circ$ ($1/\cos\theta \approx 2.9$), but the mean t/λ value is still less than 2 for the $\sim 80 \text{ nm}$ -thick films of this study.

It is worth asking whether the image contrast displayed in Figure 3 could have been obtained by conventional bright-field TEM, a technique that is better established and more widely available, given that BF-TEM can be performed without an imaging energy filter. The absence of the morphological features of Figure 3 in Figure 2C demonstrates that amplitude contrast is insufficient in the compositionally similar phases constituting the BHJ thin film. To perform a direct comparison of the contrast produced by BF-TEM phase-contrast and low-loss EFTEM spectroscopic-contrast imaging of the BHJ device structure, a series of energy-filtered images with the energy-selecting slit centered at 0 and 19 eV loss was acquired from a common area of the specimen while varying the defocus of the objective lens from $-25 \mu\text{m}$ to $+25 \mu\text{m}$ in increments of $5 \mu\text{m}$. These data are most dramatically displayed in a movie showing a side-by-side comparison of the image contrast through the focal series, which can be viewed in the Supporting Information; representative images from this series are presented in Figure 5. The EFTEM images demonstrate the necessity of performing the low-loss imaging analysis at Gaussian focus; deviation from this focus quickly effects a loss of spatial resolution. This degradation in resolution is illustrated by the two images acquired with defocus values of $-25 \mu\text{m}$ and $+25 \mu\text{m}$, in which little if any contrast remains apart from low frequency modulations arising from thickness variations. It is evident that the contrast produced by the defocused BF TEM image of this particular BHJ film is complex and dissimilar to the P3HT morphology revealed by the EFTEM imaging. This dissimilarity

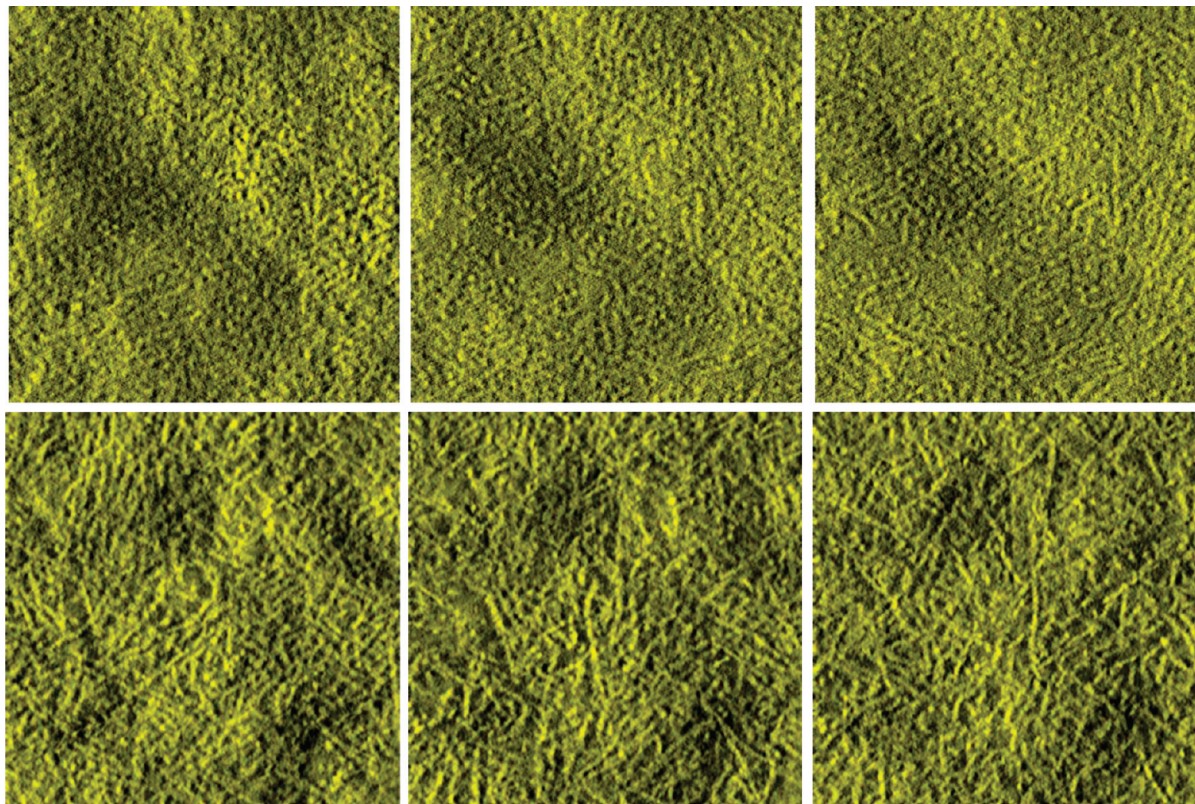


Figure 6. Array of images corresponding to the phase distributions at different depths within the BHJ, as extracted from reconstructed tomograms of P3HT:PCBM BHJ films acquired using (top) defocused ZL BF ($E = 0$ eV, $f = -25$ μm) and (bottom) in-focus EFTEM low-loss images ($E = 19$ eV, $f = 0$ μm). The slices correspond to depths (left) near the “free” surface of the film, (middle) midway through the ~ 80 nm-thick film, and (right) near the surface closest to the PEDOT:PSS-coated ITO substrate. The field of view in all images is ~ 900 nm.

is common to the BF TEM images at all defocus values, as demonstrated in the supplemental movie. While not necessarily refuting its application by other researchers to the analysis of other BHJ films, this comparison demonstrates that BF TEM imaging with a defocused objective lens is not a robust technique for the analysis of all BHJ systems generally, at least under noncryogenic conditions, and it demonstrates the relative robustness of the EFTEM technique as a means of generating contrast which faithfully depicts the chemical phase distribution within the film. A second focal series analysis was also carried out over a range of (-30 to $+30$) μm defocus using a finer increment of 1 μm , and a movie of this data set is also included in the Supporting Information.

This discrepancy in the results produced via the two imaging methods necessarily carries over into tomography studies. Two-dimensional slices of constant depth within the film, as extracted from tomographic reconstruction of tilt series acquired with imaging conditions similar to upper left and lower middle images of Figure 5, are shown in Figure 6 (a movie of the entire reconstructed volume is presented included in the Supporting Information). The slices extracted from the defocused BF tilt series suggest a three-dimensional network of P3HT filaments, consistent with the nominal microstructure of the film. However, the filament size and distribution suggested by the BF phase-contrast imaging is clearly inconsistent with that of the EFTEM spectroscopic-contrast imaging tilt series.

The reconstruction generated from the spectral-contrast data, which represents the true structure of the BHJ thin film, suggests that it consists of a highly interconnected 3D network of P3HT filaments in a PCBM matrix. No obvious preferential segregation of the phases relative to the surfaces of the thin film was detected within the resolution of the tomogram, which is on the order of

a few nanometers, since all of the slices were found to contain a similar area fraction of P3HT filaments.

It is noteworthy that, in the case of both BF and EFTEM, the tilt series data were acquired with the specimen at ambient temperature; under these conditions, the crystalline structure of the specimen rapidly degrades. Observations of the selected-area electron diffraction ring patterns of these films indicates that crystalline order of the sample breaks down after only a few seconds of exposure to the electron beam. This structural alteration would have a strong effect on the diffraction contrast contained in the BF images; however, it has negligible effect on the dielectric response revealed by EFTEM low-loss imaging. Beyond the well-known effects of film shrinkage during the first few minutes of beam exposure,³² no significant change was observed in the morphology of the phase distribution in the BHJ thin films. Some change was observed in the EELS spectrum of the BHJ during an extended period of electron exposure similar to that necessary for collecting a tomographic tilt-series. Most notably, the π -plasmon excitation peak (~ 6.6 eV) was found to decrease in intensity and shifted to a slightly lower energy-loss value over time. However, on the whole, the dielectric response of the BHJ film remains fairly constant over this prolonged period of exposure. A movie showing the response of the film to the electron beam irradiation and a plot of the EELS spectral time series data can both be found in the Supporting Information. The ability to perform tomographic studies of organic BHJ device structures in the absence of cryogenic cooling is an advantage of the spectroscopic-contrast imaging mechanism of this work; it would provide a definite advantage to this imaging mode should this beam insensitivity be generally applicable to different organic systems.

In this work, we have performed a comparison of the data generated via BF phase-contrast imaging and EFTEM spectroscopic-contrast imaging using the low-loss dielectric response. To best achieve this comparison, all of the data were acquired at 80 kV in order to maximize the contrast in the bright-field images. Both elastic and inelastic scattering cross sections decrease with increasing incident beam energy; imaging at relatively low voltages, such as 80 kV, is a common means of maximizing BF image contrast in organic specimens, since elastic scattering is enhanced and the sample is more transparent to electrons at higher accelerating voltages. However, this enhancement in contrast due to elastic scattering is not necessary for EFTEM spectroscopic-contrast imaging, and there may be significant advantages to performing tomography experiments at higher operating voltages (i.e., 200 kV–300 kV). In particular, the corresponding decrease in the inelastic scattering cross section effects an increase in λ , and thereby a decrease in t/λ for a given film thickness. For the films characterized in this study, the considerable reduction in t/λ at the highest tilt angles, from $t/\lambda \approx 2$ at 80 kV to a value closer to $t/\lambda \approx 1$ at 300 kV, would significantly decrease the nonlinear effects of plural scattering, and thereby improve the quantitative accuracy of the tomographic reconstruction, particularly for microstructural variations in the plane of the film, which are best sampled at high specimen tilts. More importantly, the increase in λ should improve the tractability of analyzing actual BHJ device structures, which have film thicknesses larger than those of the model films analyzed in this study. An increased accelerating voltage will tend to increase the effects of TEM “knock on” damage (the physical displacement of individual atoms due to elastic, billiard-ball-like interactions), but will decrease the effects of “ionization” damage (bond breaking from inelastic scattering),³² which might be more important for preserving the dielectric response that provided the spectroscopic contrast. Experiments to characterize the trade-offs of these various experimental parameters, and to maximize the reliability and information content of tomographic analysis of actual BHJ devices, will be detailed in a subsequent publication.

4. Conclusions

Low-loss EFTEM imaging is well suited to generating contrast between compositionally similar organic phases, such as those present in BHJ device structures. The plasmon-loss region of the EELS spectrum of the two-phase BHJ device is well modeled as a linear combination of the spectral responses of the individual constituent phases, and energy-filtered imaging with the energy-selecting slit transmitting a spectral range over which the component spectra exhibit significant differences in intensity provides image contrast that discriminates well between the two phases. This low-loss EFTEM signal provides a basis for electron tomography of BHJ thin films as a means to reveal the complex three-dimensional microstructure of organic photovoltaic device structures. In contrast to BF-TEM phase contrast imaging, EFTEM low loss imaging generates readily interpretable contrast that obeys the tomography projection requirement, and is particularly useful where diffraction and mass–thickness contrast are not available. In addition, the spectroscopic contrast of the EFTEM low-loss imaging is less sensitive than diffraction-based contrast to electron irradiation, thus providing a relaxation of dose requirements for the imaging of organic phases, thereby allowing tomography of thicker BHJ films to be collected at higher incident electron energies and without the need for cryogenic cooling of the specimen.

Acknowledgment. We would like to thank Drs. XinRan Zhang, Steven Hudson, and Dean DeLongchamp (NIST) for providing the samples and for many helpful discussions. A.A.H. acknowledges the support of the NRC Postdoctoral Research Associateship program.

Supporting Information Available: Online data contain a movie of the zero-loss filtered and low-loss EFTEM through-focal image series, EFTEM time series data used for the beam damage analysis, and a movie of the reconstructed tomogram. This material is available free of charge via the Internet at <http://pubs.acs.org>.

References and Notes

- (1) Lewis, N.; Crabtree, G. *Basic Research Needs for Solar Energy Utilization*; U.S. Department of Energy: Germantown, MD, 2005.
- (2) Brabec, C. *Sol. Energy Mater. Sol. Cells* **2004**, *83*, 273–292.
- (3) Liang, Y.; Xu, Z.; Xia, J.; Tsai, S.-T.; Wu, Y.; Li, G.; Ray, C.; Yu, L. *Adv. Mater.* **2010**, *22*, 1–4.
- (4) Yu, G.; Gao, J.; Hummelen, J. C.; Wudl, F.; Heeger, A. J. *Science* **1995**, *270*, 1789–1791.
- (5) Frank, J. In *Electron Tomography: Methods for Three-Dimensional Imaging of Visualization in the Cell*; Frank, J., Ed.; Springer: New York, NY, 2006; pp 1–16.
- (6) van Bavel, S. S.; Sourty, E.; de With, G.; Loos, J. *Nano Lett.* **2009**, *9*, 507–513.
- (7) Yang, X.; Loos, J.; Veenstra, S. C.; Verhees, W. J. H.; Wienk, M. M.; Kroon, J. M.; Michels, M. A. J.; Janssen, R. A. J. *Nano Lett.* **2005**, *5*, 579–583.
- (8) van Bavel, S. S.; Sourty, E.; de With, G.; Frolic, K.; Loos, J. *Macromolecules* **2009**, 7396–7403.
- (9) Hawkes, P. W. In *Electron Tomography: Methods for Three-Dimensional Imaging of Visualization in the Cell*; Frank, J., Ed.; Springer: New York, NY, 2006; pp 83–112.
- (10) Reimer, L.; Fromm, I.; Hülk, C.; Rennekamp, R. *Microsc. Microanal. Microstruct.* **1992**, *3*, 141–157.
- (11) Hunt, J. A.; Disko, M. M.; Behal, S. K.; Leapman, R. D. *Ultramicroscopy* **1995**, *58*, 55–64.
- (12) Siangchaew, K.; Libera, M. *Microsc. Microanal.* **1997**, *3*, 530–539.
- (13) Lieser, G.; Schmid, S. C.; Wegner, G. *J. Microsc.* **1996**, *183*, 53–59.
- (14) Du Chesne, A. *Macromol. Chem. Phys.* **1999**, *200*, 1813–1830.
- (15) Varlot, K. *Polymer* **2000**, *41*, 4599–4605.
- (16) Weyland, M.; Midgley, P. A. *Microsc. Microanal.* **2003**, *9*, 542–555.
- (17) Gass, M. H.; Koziol, K. K.; Windle, A. H.; Midgley, P. A. *Nano Lett.* **2006**, *6*, 376–379.
- (18) Yamauchi, K.; Takahashi, K.; Hasegawa, H.; Iatrou, H.; Hadjichristidis, N.; Kaneko, T.; et al. *Macromolecules* **2003**, *36*, 6962–6966.
- (19) Li, G.; Yao, Y.; Shrotriya, V.; Yang, Y.; Yang, H.; Yang, G. *Adv. Funct. Mater.* **2007**, *17*, 1636–1644.
- (20) Certain commercial equipment, instruments, or materials are identified in this document. Such identification does not imply recommendation or endorsement by the National Institute of Standards and Technology, nor does it imply that the products are necessarily the best available for the purpose.
- (21) Germack, D. S.; Chan, C. K.; Hamadani, B. H.; Richter, L. J.; Fischer, D. A.; Gundlach, D. J.; DeLongchamp, D. M. *Appl. Phys. Lett.* **2009**, *94*, 233303.
- (22) Schaffer, B.; Grogger, W.; Kothleitner, G. *Ultramicroscopy* **2004**, *102*, 27–36.
- (23) Kotula, P. G.; Keenan, M. R.; Michael, J. R. *Microsc. Microanal.* **2003**, *9*, 1–17.
- (24) Kremer, J. R.; Mastrorarde, D. N.; McIntosh, J. R. *J. Struct. Biol.* **1996**, *116*, 71–76.
- (25) Jackson, J. D. *Classical Electrodynamics*, 2nd ed.; John Wiley & Sons: New York, NY, 1975; p 636.
- (26) Kuzuo, R.; Terauchi, M.; Tanaka, M.; Saito, Y.; Shinohara, H. *Phys. Rev. B* **1994**, *49*, 5054–5057.
- (27) Kuzuo, R.; Terauchi, M.; Tanaka, M.; Saito, Y.; Shinohara, H. *Jpn. J. Appl. Phys.* **1991**, *30*, 1817–1818.
- (28) Kline, R. J.; McGehee, M. D.; Kadnikova, E. N.; Lie, J.; Frechet, J. M. J. *Adv. Mater.* **2003**, *15*, 15119–1522.
- (29) Kotula, P. G.; Keenan, M. R.; Michael, J. R. *Microsc. Microanal.* **2006**, *12*, 36–48.
- (30) Kotula, P. G.; Keenan, M. R. *Microsc. Microanal.* **2006**, *12*, 538–544.
- (31) Egerton, R. F. *Electron Energy-Loss Spectroscopy in the Electron Microscope*, 2nd ed.; Plenum Press: New York, NY, 1996; pp 302–303.
- (32) Egerton, R. F.; Li, P.; Malac, M. *Micron* **2004**, *35*, 399–409.